Hindawi
International Journal of Energy Research
Volume 2023, Article ID 3608634, 17 pages
https://doi.org/10.1155/2023/3608634

*Research Article*

# Improvement in the Stability of Cation (Si)/Anion (F or N) Codoped ZnO Thin-Film Transistors Formed via Atomic Layer Deposition

**Chaeseon Hong**,[1] **Minjae Kim**,[1] **Byeong-Min Lim**,[2] **Sunil Moon**,[3] **Keonwook Kang**,[3] **Ioannis Kymissis**,[4] **Hong-Sub Lee**,[2] **and Hyung-Ho Park**[1]

[1]*Department of Materials Science and Engineering, Yonsei University, Seoul 03722, Republic of Korea*
[2]*Department of Advanced Materials Engineering for Information and Electronics, Kyung Hee University, Yongin, Gyeonggi-do 17104, Republic of Korea*
[3]*Department of Mechanical Engineering, Yonsei University, Seoul 03722, Republic of Korea*
[4]*Department of Electrical Engineering, Columbia University, New York, NY 10027, USA*

Correspondence should be addressed to Hong-Sub Lee; h.s.lee@khu.ac.kr and Hyung-Ho Park; hhpark@yonsei.ac.kr

Received 3 March 2023; Revised 21 September 2023; Accepted 8 October 2023; Published 25 October 2023

Academic Editor: Tholkappiyan Ramachandran



The characteristics of cation (Si) and anion (F or N) codoped ZnO thin films formed via atomic layer deposition and corresponding device properties were investigated for different anion doping concentrations with a fixed Si doping amount. All films exhibited the (100) primary diffraction peak, indicating a hexagonal wurtzite structure. All codoped ZnO films exhibited the same effect of oxygen vacancy passivation, i.e., reduced oxygen vacancy. However, the electrical and optical characteristics of the films exhibited contrasting tendencies depending on the type of anion element. The optimized device properties, i.e., the subthreshold swing, field-effect mobility, threshold voltage, and bias stability were $6.62E-01$ V/dec, 5.10 $cm^2$/V·s, -11.16 V, and 6.32 V in the Si/F-19 condition and $5.98E-01$ V/dec, 16.60 $cm^2$/V·s, 1.07 V, and 0.14 V in the Si/N-19 condition, respectively. These characteristics were attributable to the correlation effects of the reduced interfacial trap density from Si doping and oxygen vacancy passivation from anion doping. Notably, the behavior of each anion was different in terms of the charge carrier concentration. First-principles calculations based on the density functional theory using the Vienna ab initio simulation package (VASP) code were performed to obtain valuable insights into the energy band structure in terms of the performance of the codoped ZnO films.

## 1. Introduction

Transparent semiconductor oxides (TSOs) have attracted considerable research interest owing to their promising features such as piezoelectric and magnetic properties, visible-range transparency, outstanding deposition uniformity, and high field-effect mobility, which are used in gas sensors, radiation detectors, varistors, solar cells, and switching devices [1]. Among TSOs, amorphous indium-gallium-zinc-oxide (*a*-IGZO) has been commercialized and successfully applied in the display industry and other related domains [2]. However, *a*-IGZO contains a large amount of In, which is toxic and not abundantly available. Moreover, *a*-IGZO exhibits persistent photoconductivity, i.e., a negative threshold voltage ($V_{th}$) shift under negative bias and illumination stress (NBIS) conditions. The large negative shift in $V_{th}$ over prolonged bias stress is usually attributable to oxygen valency ($V_O$) [3]. These aspects may degrade the operating characteristics of the devices and their products. Moreover, field-effect mobility ($\mu_{FE}$) must be enhanced to realize next-generation ultrahigh-resolution displays such as those for virtual and augmented reality [4]. Therefore, In-free alternatives with high

field-effect mobility and more stable $V_{th}$ reliability in stress conditions must be identified for next-generation future displays. To this end, a promising strategy is the extrinsic doping of ZnO.

Many researchers have attempted to introduce various elements to enhance the properties of ZnO. Al-doped ZnO is widely used in thin-film photovoltaic techniques and has largely replaced In-oriented TCOs [5]. However, Al-ZnO is susceptible to moisture, which prevents its widespread use [6]. Another promising alternative is Ga-doped ZnO. However, the electrical conductivity of the corresponding thin films decreases significantly after damp heating, resulting in deteriorated optoelectronic device performance [7]. In this context, the performance of single-doping materials must be enhanced to promote their application to a broader range of products. Codoping into ZnO, such as Ga/F, Co/Mn, Al/N, Fe/Co, and Na/Mg, is a potential strategy to achieve this goal [8–12].

As a promising cation candidate, Si functions as an effective donor in films prepared by magnetron sputtering deposition [13]. Si has an atomic size of 1.11 Å, comparable to that of Zn (1.22 Å) [14], and thus, the use of Si as a dopant in ZnO can reduce the lattice mismatch [15]. Moreover, the Si element is nontoxic to humans and abundant in the Earth's crust. Therefore, it can be more easily commercialized compared with elements such as In, Ga, and Sn. Si forms tail states underneath the conduction band minimum (CBM) and can enhance the carrier concentration and resistivity (i.e., conductivity) of the thin film [16]. In terms of the anion, it is valuable to compare the characteristics of nitrogen (N) and fluorine (F) within the same period (II) centered on O. Because both elements are capable of oxygen vacancy passivation, the influence of the anion valence change and doping concentration on the thin film and device performance must be clarified. In general, F ions can constrain electron scattering in the conduction band by suppressing electronic perturbation at the O substitution site [17]. Similar to the cation dopant, F ions can enhance the film mobility and decrease the resistivity. Additionally, the size of F ions is comparable to that of O ions ($F^{1-}$: 1.31 Å and $O^{2-}$: 1.38 Å) [8], and thus no lattice distortion occurs when doped in the ZnO films. N has been considered to be an effective p-type dopant for ZnO, and its ionic radius is comparable to or slightly larger than oxygen ($N^{3-}$: 1.46 Å and $O^{2-}$: 1.38 Å) [18, 19]. Moreover, it exhibits the lowest ionization energy between all group V elements, enabling the realization of a shallow acceptor level in ZnO [20]. Therefore, F or N can be used as anions to control the acceptor level above the valence band maximum (VBM) [21].

Various techniques can be used to deposit ZnO, such as sol–gel, radio frequency sputtering, physical/chemical vapor deposition, and atomic layer deposition (ALD). Among them, ALD can produce high conformality and atomic-scale precision with respect to the film thicknesses, as well as outstanding interfacial properties between the channel and insulator owing to its self-limiting behavior at low temperatures and is thus a promising deposition technology for thin film transistors (TFTs) on various substrates [22–24]. Doping in semiconductor materials via atomic layer deposition (ALD) involves the controlled introduction of specific elements such as silicon (Si), nitrogen (N), and fluorine (F) to modify their electrical properties. Si doping utilizes tris(dimethylamino)silane (TDMAS, $Si[N(CH_3)_2]_4$) as a precursor to adjust carrier concentration, enabling the creation of n-type regions in semiconductor devices like transistors, which are essential components in electronic circuits [25]. On the other hand, F or N doping uses ALD to introduce fluorine or nitrogen atoms, typically as an acceptor impurity, to reduce carrier concentration and decrease conductivity (p-type doping) [17, 26]. This complements n-type regions and facilitates the development of p-type regions in semiconductor devices, enabling their integration into electronic circuits.

Considering these aspects, this study examines the structural, electrical, optical, and stability characteristics of thin films and devices fabricated through the codoping of Si (for controlling the CBM region) and F or N (for controlling the VBM region). Because Si as a multivalent dopant has a significant donor effect compared with the other elements, its doping concentration was limited to approximately 1 at% considering charge carrier saturation and scattering. Figure S1(a) shows the relationship between ZnO and the selected dopants, i.e., the cation (Si) and anion (F or N).

## 2. Experimental

*2.1. Material Deposition and Device Fabrication.* The codoped ZnO thin films were deposited on $SiO_2$ (100 nm)/Si (p-type, 100) substrates and liquid crystal display glass (Fusion 1737) substrates via ALD at a substrate temperature of 150°C and working pressure of 1 Torr by using a traveling-wave-type Lucida D100 system (NCD Technology, Inc., Korea). Diethylzinc (DEZ; EG Chem. Co., Ltd., Korea), diluted hydrogen fluoride ($HF/H_2O$, 49–51%, HF; DUKSAN Chem., Co., Ltd., Korea, diluted in deionized (DI) water), diluted ammonium hydroxide ($NH_3/H_2O$, 28–30%, $NH_3$; DUKSAN Chem., Co., Ltd., Korea, diluted in DI water), and DI water were used as the Zn precursor, F dopant, N dopant, and O precursor, respectively. The Si source for doping into ZnO was tris(dimethylamino)silane (TDMAS: $(Me_2N)_3SiH$, Hansol Chemical Co., Ltd., Korea). DEZ was chilled at 10°C and delivered into the reaction chamber at a flow rate of 20 sccm with high-purity $N_2$ (99.999%) as the carrier gas. TDMAS was heated at 60°C to provide adequate vapor pressure without any condensation. $HF/H_2O$ and $NH_4OH/H_2O$ were preserved at room temperature, and the flow rates were the same as those for DEZ.

The anion source, i.e., $HF/H_2O$ or $NH_3/H_2O$, and $H_2O$ were alternatively injected with a regulated Zn-O : Zn-O/F or N ratio to integrate the selective anion doping concentration into Si-doped ZnO films. The Si doping concentration was set at 1 : 19 ($SiO_X$_1 cycle : ZnO_19 cycle), whereas the anion doping concentration was varied from 4 to 19. The sample was labeled according to the cycle condition based on the ALD deposition process shown in Figure S1(b). For example, Si-ZnO (1 : 19) indicates Si-doped ZnO with a ratio of 1 : 19 (i.e., $SiO_X$_1 cycle : ZnO_19 cycle). Si-F-ZnO (1 : 4 : 15) represents Si/F codoped ZnO with a ratio of 1 : 4 : 15 (i.e., $SiO_X$_1 cycle : F-doped ZnO_4 cycle : ZnO_15 cycles). Si-N-ZnO was labeled in a similar manner, and all conditions are summarized in Table 1.

All the conditioned films were postannealed for 1 h at 400°C in an oxygen environment after the deposition. A bottom-gated TFT device with a channel width (W) of 100 $\mu$m and length (L) of 5 $\mu$m was fabricated using a mask aligner (M-150, Pro Win Co., Ltd., Korea). A 4 nm-thick adhesion layer (Ti) and 30 nm-thick source/drain electrode (Au) were deposited using an e-beam evaporator. Figures 1(a) and 1(b) show the device structure view and the uniformity results from atomic force microscopy (AFM).

*2.2. Thin Film and Device Characterization.* The crystallinity of codoped ZnO thin films formed with ALD supercycles was examined by X-ray diffraction (XRD; D/MAX-2000, Rigaku, Japan) with a Cu–K$\alpha$ radiation source ($\lambda = 1.5418$ Å) and operating parameters of 40 kV and 30 mA. The film thickness was verified through ellipsometry (GAERTNER, L117 C, USA). Electrical properties, such as the resistivity ($\rho$), carrier concentration ($n$), and Hall mobility ($\mu_H$), were measured at room temperature using a Hall effect data acquisition system based on the van der Pauw method (Ecopia, HMS-3000, Korea). The optical transmittance in the 200–900 nm range was measured using an ultraviolet-visible-near infrared (UV-vis-NIR) spectrophotometer (V-570, JASCO, Japan). X-ray photoelectron spectroscopy (XPS; K$\alpha$, Thermo Scientific Inc., UK) with monochromatic Al X-ray sources (Al k line: 1486.6 eV) and operating parameters of 12 kV and 3 mA was performed to analyze the surface elemental composition of the films. The current-voltage (I-V) characteristics of the prepared devices were determined using a Keithley 2636B (USA) source meter.

*2.3. Simulation.* The Vienna ab initio simulation package (VASP) code was used to perform first-principles calculations based on the density functional theory (DFT), using the Perdew–Burke–Ernzerhof exchange-correlation function with generalized gradient approximation [27–30]. In general, calculations based on DFT-LDA or DFT-GGA invoke the well-known bandgap underestimation error, and thus, appropriate corrections must be introduced, i.e., the Hubbard $U$ parameter with the $p$-orbital of O ($U_p = 7$ eV) and $d$-orbital of the transition metal ($U_d = 10$ eV) [16]. The coupling in both the Zn 3d states and O 2p states causes the top of the valence band to move upward, eventually lowering the bandgap [31]. In this study, the cases of doping or codoping with Si, F, and N into ZnO were explored using a $3 \times 3 \times 2$ supercell containing 36 Zn atoms and 36 O atoms. The energy cutoff of 340 eV and a self-consistent field tolerance of $1.0 \times 10^{-6}$ eV were used. Brillouin's zone integration was performed using $2 \times 2 \times 1$ k-points and the Monkhorst–Pack approximation.

## 3. Results and Discussion

*3.1. Crystalline Structure and Growth Orientation.* Figures 2(a) and 2(b) show the XRD results for Si-F-ZnO and Si-N-ZnO films with varying F or N doping concentrations and constant Si doping concentrations. All films exhibit a hexagonal wurtzite crystalline structure, with a high-intensity peak at 31.93 (100) and other peaks at 34.39 (002), 36.26 (101), and 56.68 (110), consistent with the reference code JCPDS 96-210-7060.

In general, ZnO has a preferred orientation for (002) in which the surface energy is lower than that in other planes [32]. The (100) preferred orientation in this study, however, could be attributed to the following reasons: the deposition temperature highly influences the crystal orientation for ALD-derived ZnO thin films [33]. Pung et al. observed that (100) and (002) oriented crystals are prominent in films obtained below 150°C, then the (100) orientation becomes dominant at temperatures between 150 and 220°C, and thus the (002) orientation becomes dominant at temperatures above 220°C. These unique orientation growth properties are well explained by the hindering process suggested by Baji et al. [34]. The distance between hydroxyl groups distributed onto the surface is 5.2 Å for (100) and 3.25 Å for (002), and the Zn-Et bond length of DEZ is 1.95 Å. Therefore, the molecules have enough space to adhere in the (100) direction without steric barriers. On the other hand, the reversal growth change from (100) to (002) is attributed to exposure to an oxygen-rich environment, such as $H_2O_2$, or a higher oxygen flow rate [35].

After Si doping, FWHM increases, grain size decreases, and lattice strain increases, implying that the crystallinity of Si-ZnO was degraded when compared to ZnO. Also, it can be said that the grain size decreases and the lattice strain increases in the case of F or N codoping, which is similar to the case of Si-ZnO. The grain size and interplanar distance were calculated using the following equations [36]:

$$D = \frac{K\lambda}{\beta \cos \Theta}, \tag{1}$$

$$\frac{1}{d^2} = \frac{4}{3} \bullet \left( \frac{h^2 + hk + k^2}{a^2} \right) + \frac{l^2}{c^2}, \tag{2}$$

where $\beta$ is the FWHM of the peak, $K$ is the shape factor (=0.9), $\lambda$ is the wavelength of Cu–K$\alpha$ in Eq. (1), and $h$, $k$, and $l$ in Eq. (2) are the Miller indices. The results are summarized in Table S1. Moreover, the film thickness from the ellipsometry is similar in all codoping cases, as shown in Figure S2: (a) 35.21 ± 3.48 nm for Si-F-ZnO and (b) 35.25 ± 2.28 nm for Si-N-ZnO, respectively.

In conclusion, it is possible to observe the electrical and optical properties of the thin film and its device characteristics in a state where the change in crystallinity of the thin film due to doping is minimized.

*3.2. XPS Results.* Figure 3 shows the XPS results for each core level for Si-F-ZnO and Si-N-ZnO films with increasing F or N doping concentrations and a fixed Si doping concentration. The charging effect of all spectra was compensated by using C 1s at 284.5 eV [37].

As shown in Figures 3(a) and 3(e), the Zn 2p peak does not shift and is the same (1021.0 ± 0.5 eV) for Si single doping or Si-F or Si-N codoping into ZnO [38]. In other words, secondary phases such as zinc silicates (e.g., $Zn_xSi_yO_z$ : Zn $2p_{3/2}$-1023.0 ± 0.5 eV) [39], zinc fluoride (1023 ± 0.5 eV)

Table 1: The sample label condition with $SiO_X$, F-ZnO, N-ZnO, and ZnO pulsed cycle ratio.

| Target film | Cycle ratio | Label | Pulsed materials | | | |
|---|---|---|---|---|---|---|
| | | | $SiO_X$ | F-ZnO | N-ZnO | ZnO |
| ZnO | ZnO | - | - | - | - | 20 cycle |
| Si-ZnO | Si-1/20 | 1 : 19 | 1 cycle | | - | 19 cycle |
| Si-F-ZnO | Si/F-4 | 1 : 4 : 15 | 1 cycle | 4 cycle | - | 15 cycle |
| | Si/F-9 | 1 : 9 : 10 | 1 cycle | 9 cycle | - | 9 cycle |
| | Si/F-12 | 1 : 12 : 7 | 1 cycle | 12 cycle | - | 7 cycle |
| | Si/F-19 | 1 : 19 : 0 | 1 cycle | 19 cycle | - | - |
| Si-N-ZnO | Si/N-4 | 1 : 4 : 15 | 1 cycle | - | 4 cycle | 15 cycle |
| | Si/N-9 | 1 : 9 : 10 | 1 cycle | - | 9 cycle | 9 cycle |
| | Si/N-12 | 1 : 12 : 7 | 1 cycle | - | 12 cycle | 7 cycle |
| | Si/N-19 | 1 : 19 : 0 | 1 cycle | - | 19 cycle | - |

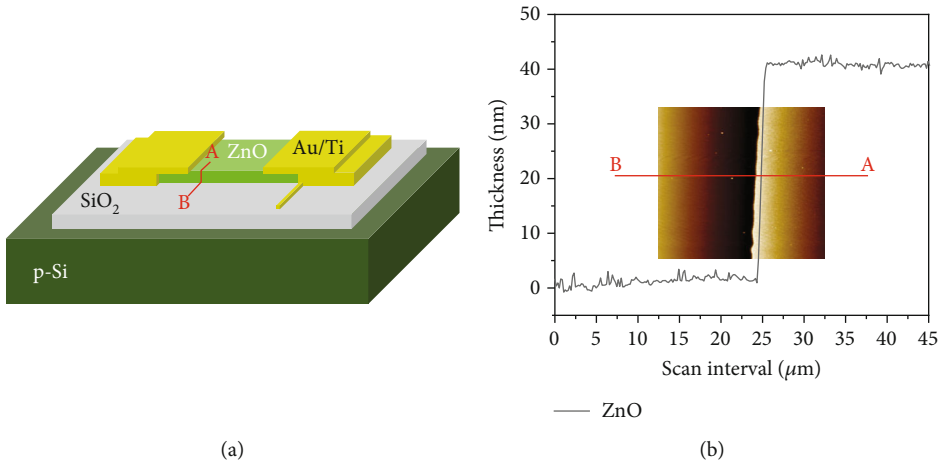


Figure 1: (a) Bottom gated device structured onto a highly doped p-type silicon wafer. (b) The device uniformity and thickness by atomic force microscopy (AFM).

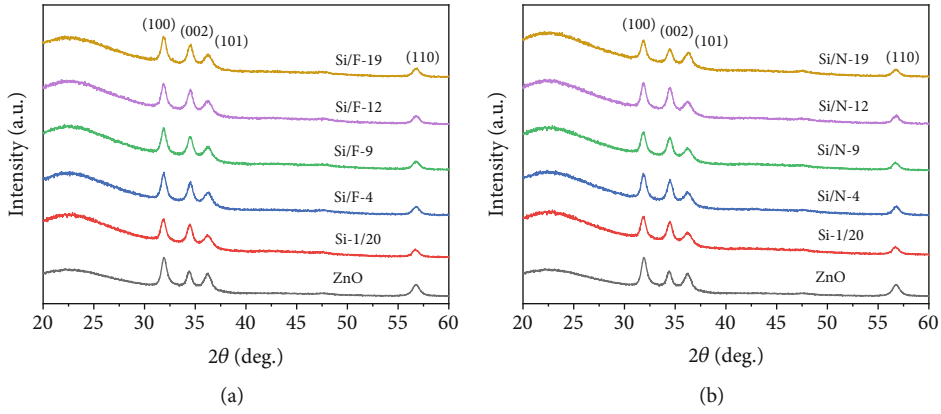


Figure 2: Crystalline characteristics for (a) Si-F-ZnO and (b) Si-N-ZnO configurations with increasing anion doping amounts at a given Si doping concentration.

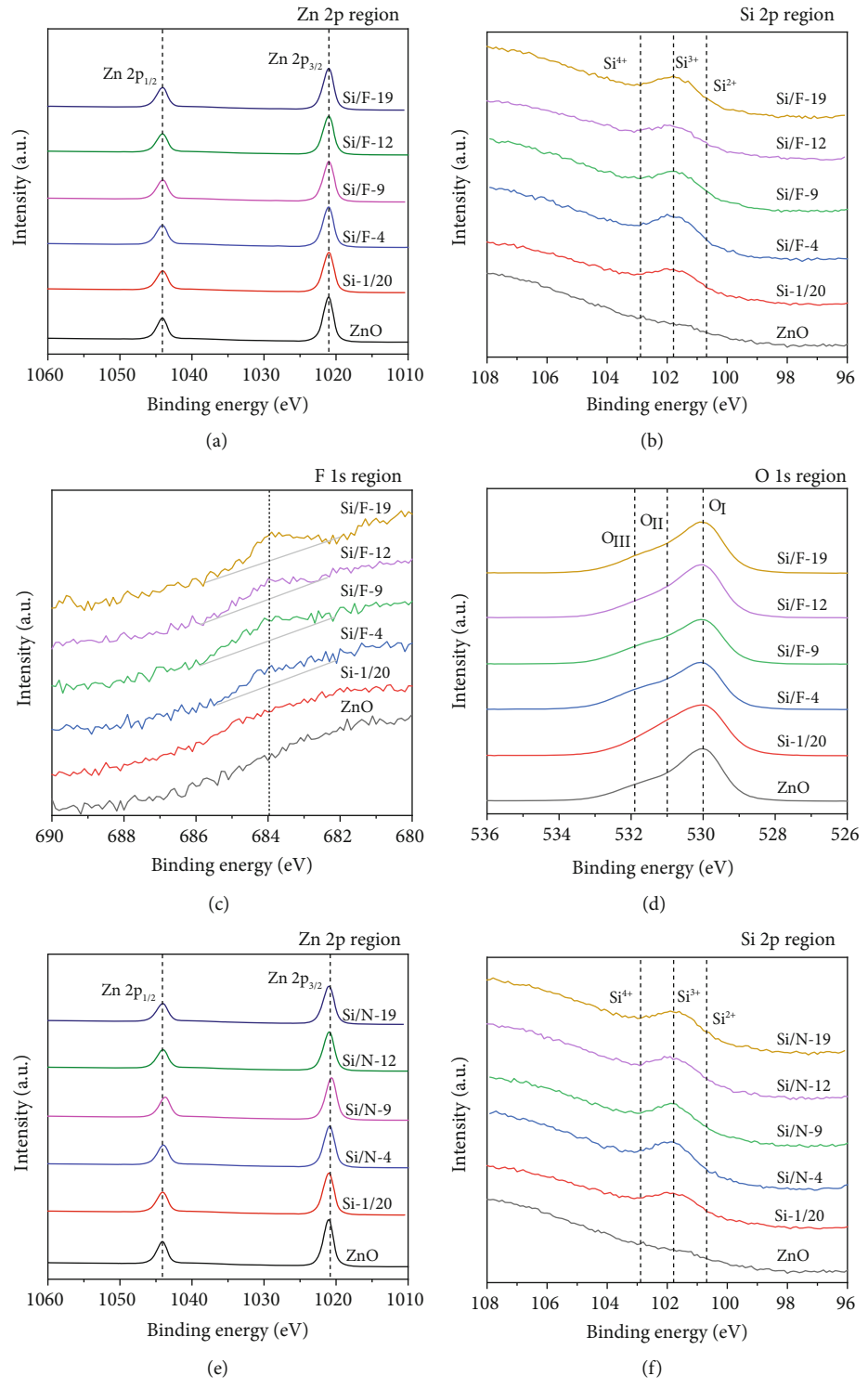


Figure 3: Continued.

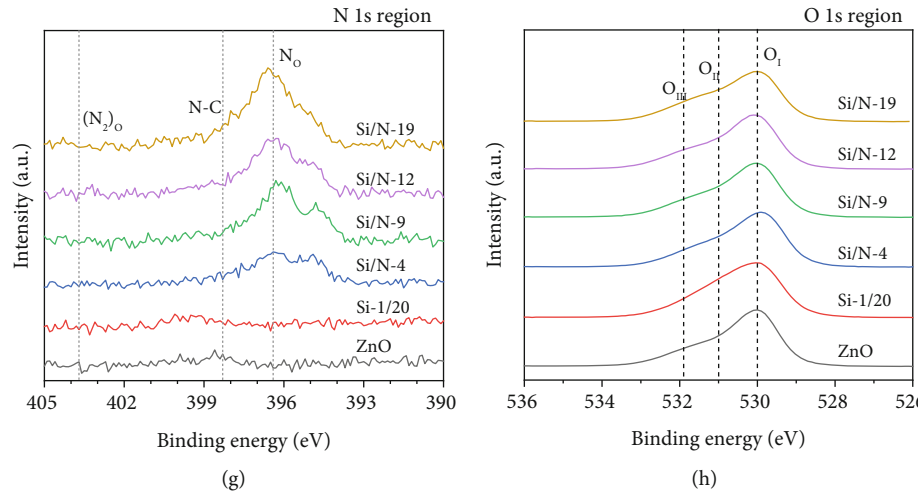


FIGURE 3: XPS spectra for the Si-F-ZnO case: (a) Zn 2p, (b) Si 2p, (c) F 1s, and (d) O 1s and Si-N-ZnO case: (e) Zn 2p, (f) Si 2p, (g) N 1s, and (h) O 1s.

[40], or zinc nitride ($1023 \pm 0.5$ eV) are not formed in the thin films [41].

Figures 3(b) and 3(f) show the Si 2p XPS spectra for Si-F-ZnO and Si-N-ZnO thin films. The Si concentration is identical in all conditioned films because the ratio of $SiO_X$ : ZnO is fixed at 1 : 19 cycles. Moreover, deconvoluting the Si 2p core level yields three subordinate chemical states corresponding to $Si^{4+}$ (103.2 eV; $SiO_2$), $Si^{3+}$ (102.1 eV; $Si_2O_3$), and $Si^{2+}$ (101.0 eV; SiO) [42]. Theoretically, the Si atom is ionized into the charge state $Si^{4+}$ in the ZnO thin film and subsequently donates two electrons [43]. However, Si has been ionized in the form of $Si^{3+}$ states in Zn sites (high intensity) and generates one electron. The state of $Si^{4+}$ is energetically unstable for the accumulation of the positive charge at the Si ions after the first one-electron donation [44]. Also, this condition has the highest defect formation energy from the first-principle calculations, implying that the $Si^{4+}$ state rarely occurs in real films [45]. Therefore, the defect equation for Si substitution in ZnO can be expressed as follows [44]:

$$Zn^{2+} \xrightarrow{Si^{3+}} Si_{Zn}^{2+} + e^{-}. \quad (3)$$

The concentration of F or N shown in Figures 3(c) and 3(g) increases monotonically as the cycle of pulses varies while the Si precursor remains constant. Table 2 summarizes the atomic concentrations of Zn, O, Si, F, and N for the ZnO, Si-ZnO, Si-F-ZnO, and Si-N-ZnO thin films. Especially, the F dopant cannot be detected in the Si-F-ZnO (1 : 4 : 15) condition as its concentration is lower than the limits of detection of the XPS instruments. The estimated concentration of F dopant is 0.3–0.5 at%, considering the concentration trend line in the obtained films.

Figures 3(d) and 3(h) show the O 1s spectroscopy results for the Si-F-ZnO and Si-N-ZnO thin films. O 1s can be classified into the three chemical states of $O_I$, $O_{II}$, and $O_{III}$, which represent the oxide lattice with Zn ($530 \pm 0.3$ eV), oxygen vacancies ($531.0 \pm 0.3$ eV), and hydroxide ($531.9 \pm 0.3$ eV), respectively [46]. As shown in Table S2, the ratio of $O_{II}/O_I$ in Si-ZnO is higher than that of ZnO after Si doping, i.e., $V_O$ increases. Previous reports confirmed that an oxygen-deficient region ($V_O$) is increased in Si-doped ZnO due to the consumption of lattice oxygen atoms within ZnO. Therefore, after Si doping, the defects for electron donation by the oxygen vacancies can be expressed as [44, 46–48]

$$O^{2-} \xrightarrow{Si^{3+}} SiO_2 + V_O + e^{-}. \quad (4)$$

Equations (3) and (4) are essentially the same for the formation process and include $Si_{Zn}O_2$, $V_O$, and one electron generation, which represent the combined structure of Si substituted in the Zn site and surrounding O. Therefore, Equations (3) and (4) can be summed to obtain

$$Zn^{2+} + O^{2-} \xrightarrow{Si^{3+}} Si_{Zn}O_2 + V_O + e^{-}. \quad (5)$$

Moreover, the oxygen vacancy transforms to the ionized state owing to light and thermal excitation and donates an electron as [3]

$$V_O \longrightarrow V_O^{2+} + \frac{1}{2}O_2 + 2e^{-}. \quad (6)$$

Thus, the final expression for the case of Si doping is

$$Zn^{2+} + O^{2-} \xrightarrow{Si^{3+}} Si_{Zn}O_2 + V_O^{2+} + \frac{1}{2}O_2 + 3e^{-}. \quad (7)$$

This condition is considered to be cation dominant and located below the CBM (Figure S1(a)).

In contrast, in the F or N codoping cases, the $O_{II}/O_I$ ratio is lower than that for Si-ZnO (Table S2). This decreasing tendency is related to the passivation effect of the oxygen vacancies caused by F or N doping [17, 49]. The O 1s spectra were normalized for the $O_I$ peak to verify the passivation efficiency between the two anion elements (Figure S3), and their results are shown in Figure 4. As you

Table 2: Concentration (at%) of the constituent components including Si, F, N, Zn, and O for ZnO, Si-ZnO, Si-F-ZnO, and Si-N-ZnO samples.

| Condition | Cycle ratio | Concentration (at%) | | | | |
|---|---|---|---|---|---|---|
| | | Si | F | N | Zn | O |
| ZnO | - | - | - | - | 45.68 | 54.32 |
| Si-ZnO | Si-1/20 | 1.49 | - | - | 44.77 | 53.74 |
| Si-F-ZnO | Si/F-4 | 1.57 | Undetected | - | 41.24 | 55.18 |
| | Si/F-9 | 1.79 | 0.76 | - | 41.74 | 55.28 |
| | Si/F-12 | 1.56 | 1.06 | - | 45.46 | 52.98 |
| | Si/F-19 | 1.68 | 1.52 | - | 44.34 | 53.99 |
| Si-N-ZnO | Si/N-4 | 1.62 | - | 1.13 | 44.41 | 52.84 |
| | Si/N-9 | 1.71 | - | 1.48 | 42.66 | 53.45 |
| | Si/N-12 | 1.53 | - | 1.60 | 43.20 | 53.37 |
| | Si/N-19 | 1.66 | - | 2.26 | 43.07 | 53.72 |

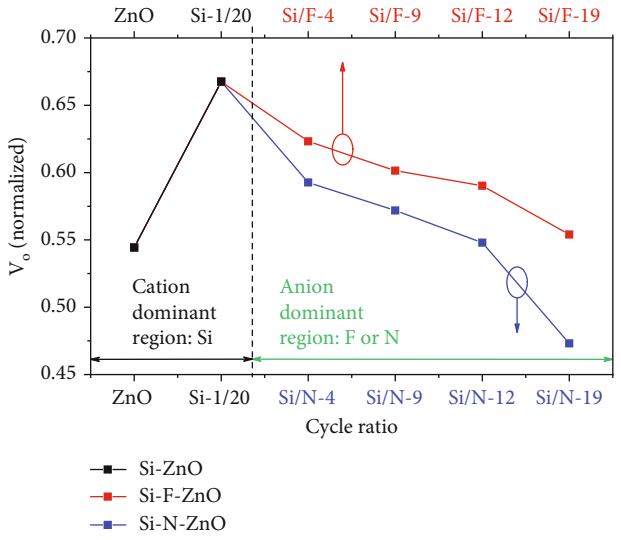


Figure 4: Normalized intensity of $V_O$ in the O 1s peak for the cation dominant region (ZnO and Si-ZnO) and anion dominant region (Si-F/N-ZnO) with increasing anion doping concentration and a fixed Si doping amount.

can see, the slope for the N codoping cases is steeper than that for the F codoping cases. These findings could be explained by the fact that $V_O$ is affected by the anion doping effect. While F or N occupy the $V_O$ position structurally, these elements can effectively passivate the neutral oxygen vacancy and release the charge carrier [50]. Therefore, it means that the passivation efficiency for N might be slightly higher than that for F in the Si-ZnO system. Therefore, the F or N codoping situation might be considered to be anion dominant and located above the VBM (Figure S1(a)). The substitution equations in the case of F or N codoping are [51, 52]

$$V_O^{2+} + 2e^- \xrightarrow{F^{1-}} F_O^{2+} + 1e^-,$$
$$V_O^{2+} + 2e^- \xrightarrow{N^{3-}} N_O^{2+} + 1h^+. \quad (8)$$

These equations indicate that both F and N exhibit a passivation effect with respect to $V_O$ but differ in terms of the charge carrier donation. Therefore, F or N codoping would be expected to have different thin film and device characteristics.

*3.3. Optical Properties.* UV-vis analysis was performed to verify the optical properties of the Si-F-ZnO and Si-N-ZnO thin films. The average transmittance (Figures S4(a) and S4(b)) in the visible range (400–800 nm) is 81.46%, 81.77%, 82.17%, and 81.43% for ZnO, Si-1/20, Si-F-ZnO, and Si-N-ZnO, respectively, with the absorption edge lying between 300 and 400 nm. These transmittance values are sufficient for commercial products such as solar cells and transparent electrodes [53].

Figures S4(c) and S4(d) show the optical bandgap of each film. Tauc's equation expresses the relationship in terms of the optical bandgap ($E_{g\_opt}$) and absorption edge ($\alpha$) [54].

$$\alpha h\nu^n = C\left(h\nu - E_g\right), \quad (9)$$

where $n = 2$ for materials with a direct bandgap, $C$ is a constant, and $h\nu$ is the photon energy. The absorption coefficient is calculated using the Beer–Lambert formula [55].

$$\alpha = \frac{1}{t} \bullet \left[\ln\left(\frac{1}{T_r}\right)\right]. \quad (10)$$

where $t$ and $T_r$ are the film thickness and transmittance, respectively. Figure 5 shows the bandgap values calculated by extrapolating the fit of the linear region to $\alpha = 0$ from the $\alpha h\nu^2$ versus $h\nu$ plot.

As shown in Figure 5, $E_{g\_opt}$ for the Si-1/20 case (cation dominant region) is higher than that of ZnO owing to the Burstein–Moss (BM) effect [44]. $E_F$ shifting above the CBM owing to the BM effect is attributed to the increased carrier concentration, which will be discussed in the section on electrical properties. Generally, $E_{g\_opt}$ is defined as the

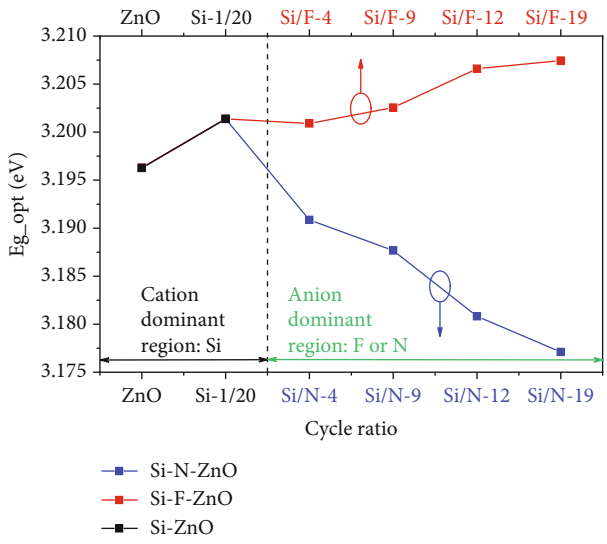


Figure 5: Optical bandgap results based on Tauc's plot for the cation dominant region (ZnO and Si-ZnO) and anion dominant region (Si-F/N-ZnO) with increasing anion doping concentration and a fixed Si doping amount is fixed.

minimum energy required to excite an electron in the valence band up to the conduction band bottom [56].

Notably, $E_{g\_opt}$ in the Si-F-ZnO and Si-N-ZnO cases exhibits opposing tendencies: the bandgap of Si-F-ZnO is greater than that of Si-ZnO, and vice versa in Si-N-ZnO. The increase in $E_{g\_opt}$ in Si-F-ZnO is attributable to the higher carrier concentration induced by F codoping into the Si-ZnO films, which strengthens the BM effect in Si-F-ZnO. The occurrence of the BM effect in F-doped ZnO thin films has been widely reported [17, 57]. However, $E_{g\_opt}$ in Si-N-ZnO decreases because $E_F$ does not shift upward as the carrier concentration decreases. In other words, the decrease in bandgap with increasing N concentrations cannot be explained by a decrease in carrier concentration; therefore, another factor, such as changes in band structure, must be considered. To verify the band structures, we systematically calculated the density of states by first-principle DFT using the VASP code.

*3.4. First-Principle Calculation: Density of States.* Figures S5(a)–S5(f) show $3 \times 3 \times 2$ supercell structures with different numbers of F or N atoms, with one atom of Si. A Si-doped ZnO supercell was generated by the substitution of one Zn atom for one Si atom. In the F or N substitution-based supercell, one oxygen atom was swapped by the anion. The atomic positions did not change with the increasing number of substituted elements. After the geometry optimization for the ZnO supercell, the crystalline lattice parameter is $a/b = 3.266$ Å; $c = 5.265$ Å, and the bandgap is 3.23 eV at the high symmetry point ($\Gamma$ point). This framework corresponds to a direct bandgap semiconductor. The results are summarized in Figure S6. The optimized calculation results are consistent with the XRD and optical Tauc's plot results.

Figures 6(a)–6(f) show the density of states to analyze the orbital distributions for ZnO, Si-ZnO, Si-F-ZnO, and Si-N-ZnO. The Fermi energy level ($E_F$), which approaches zero, is represented by a dotted line. The conduction and valence bands for ZnO are shown in Figure 6(a). The valence band of ZnO consists of two parts: the lower energy part from −8.78 to −5.52 eV consists of Zn 3d and O 2p orbitals, and the higher energy part from −5.33 to 0 eV is dominated by O 2p orbitals. The main components within the conduction band correspond to the Zn 4s and O 2p orbitals. Therefore, from the linear combination of atomic orbitals theory (LCAO), the bonding states (symmetric) are formed in the valence band region, and the antibonding states (antisymmetric) are formed in the conduction band region [58].

The Si 3s and Si 3p orbitals in the Si-ZnO supercell form the shallow donor states near $E_F$ after one Si atom is substituted for one Zn atom (Figure 6(b)). These shallow donor states help enhance the conductivity of the films. The $E_F$ of Si-ZnO shifts upward and is located above the CBM, resulting in an n-type degenerate semiconductor. This semiconductor configuration exhibits an intensified BM effect, as discussed in the section on optical properties.

Comparing Figures 6(b) and 6(c), there is little difference in TDOS shape. Although F is an anion, the results of this study show that it behaves like a cation in terms of electron donation similar to Si. Therefore, it is acceptable that CBM would be changed after F doping, but this change is very small or insignificant, which could be attributed to the minima perturbation effect on CBM. Figures 6(c) and 6(d) show that the results for the Si/F codoping case are similar to those of Si-ZnO. The band structure also does not change significantly, and F 2p and F 2s, similar to Si, influence the conduction band structures. The formation of tail states near the conduction band increases the carrier concentration and widens the $E_g$ of Si/F-ZnO compared to those of ZnO and Si-ZnO. Therefore, the F dopant replaced at the O sites in ZnO is expected to limit the perturbation of the conduction band [52]. In other words, the many-body effect in the conduction band of F-ZnO films is weakened, despite the $E_F$ of the films being shifted to the conduction band.

A new state of N 2p ranging between -1.04 and 0.69 eV is formed above the valence band by N codoping into the Si-ZnO supercell, as shown in Figures 6(e) and 6(f). As the number of N atoms increases, the DOS for N 2p increases, and the $E_g$ of the thin film decreases. Furthermore, because the N 2p orbital has more energy than the O 2p orbital, the additional N 2p states raise the VBM [21]. The localized energy regions of the unionized $V_O$ are blocked by this upward expansion of the valence band, and thus, $V_O$ ionization (i.e., electron donation) is suppressed even if thermal, light, or bias stress is applied to the films.

*3.5. Electrical Properties.* Figure S7 shows the electrical properties of the Si-F-ZnO and Si-N-ZnO thin films, based on Hall effect measurements in the van der Pauw geometry. The carrier concentration increases from $0.94 \times 10^{20}$ to $1.41 \times 10^{20}$ cm$^{-3}$ after Si doping into the ZnO thin film. Consequently, the resistivity decreases from $2.44 \times 10^{-2}$ to $2.11 \times 10^{-2}$ Ω·cm. The increased carrier scattering possibility decreases the Hall mobility from 3.01 to

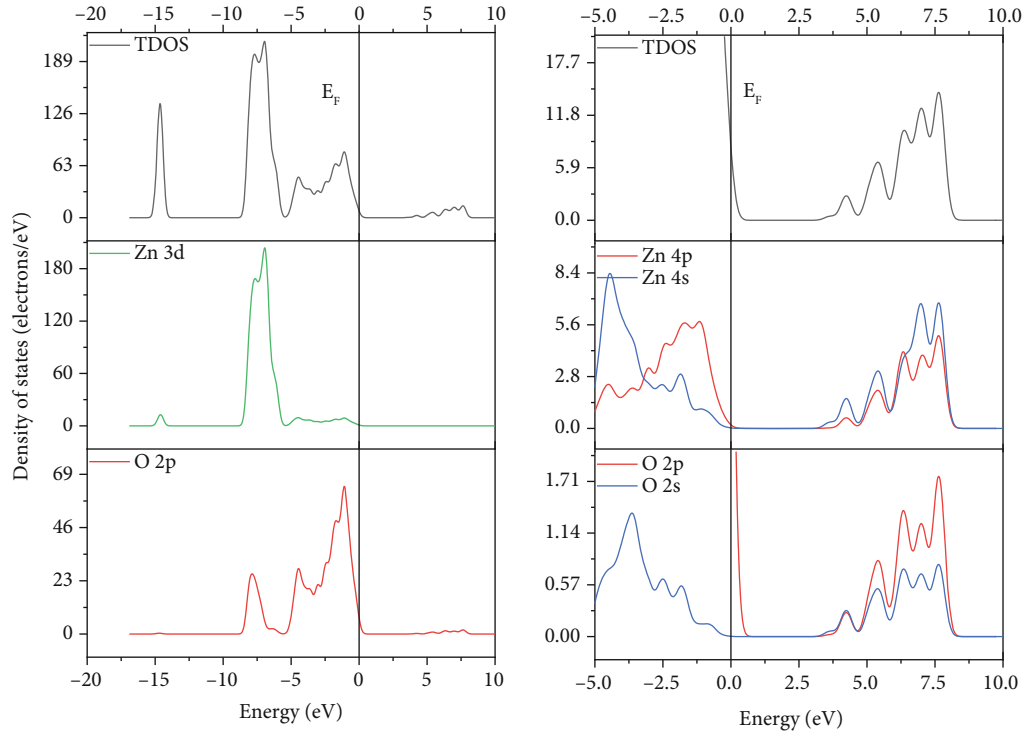


(a)

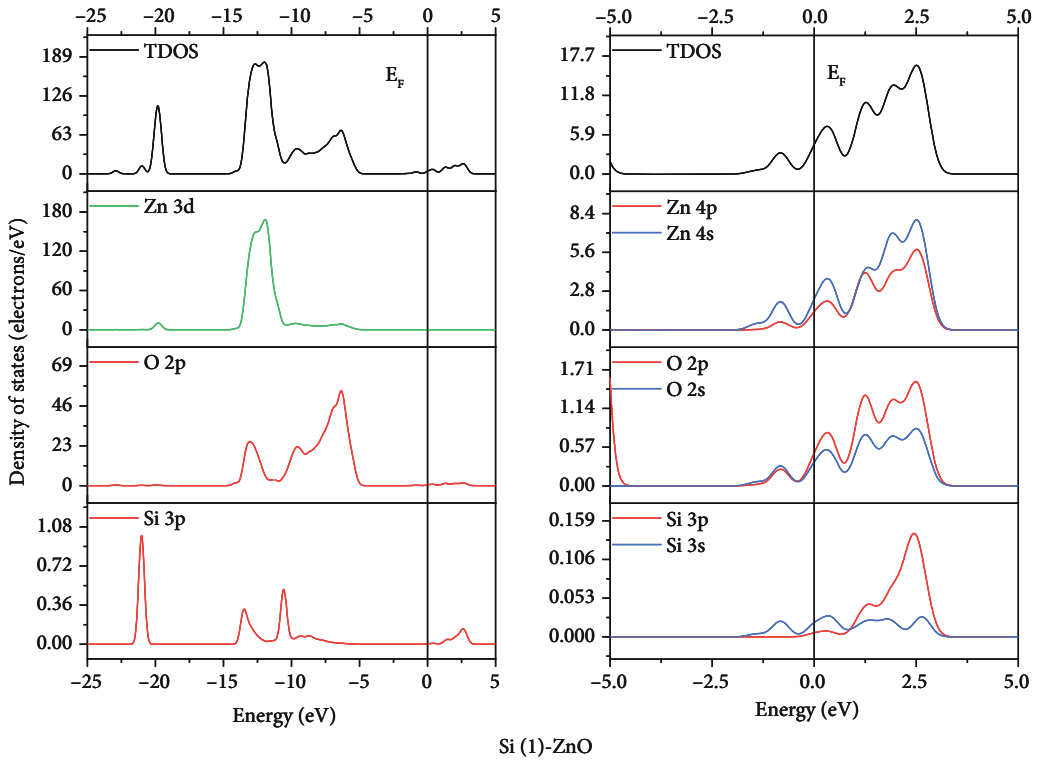


(b)

Figure 6: Continued.

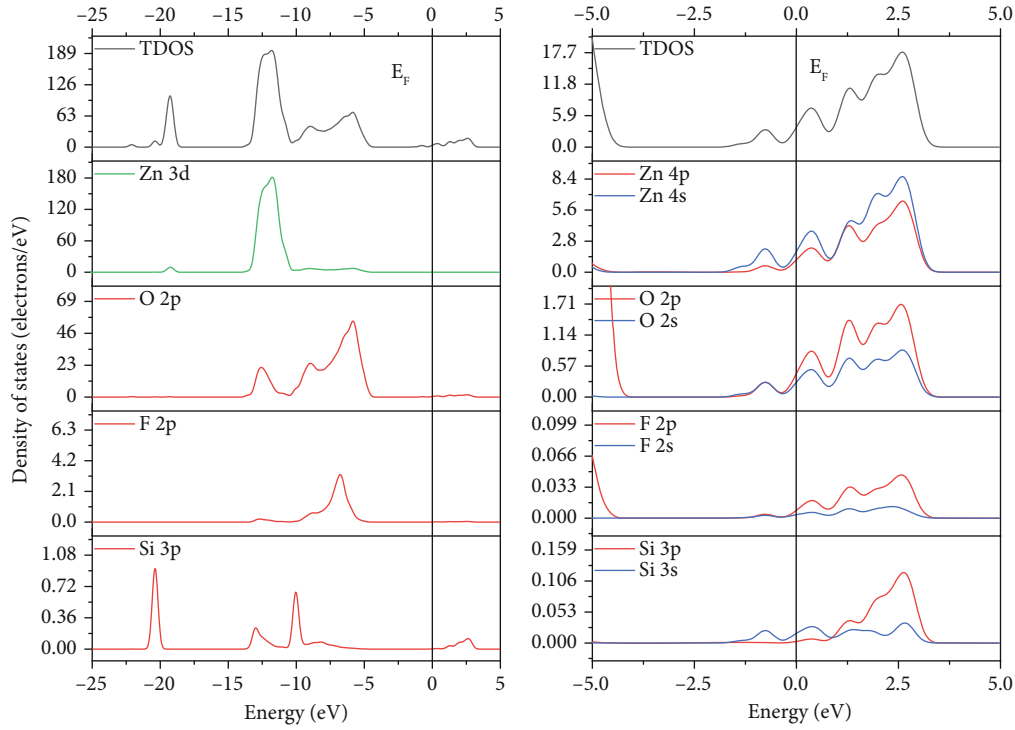


Si (1)-F (1)-ZnO

(c)

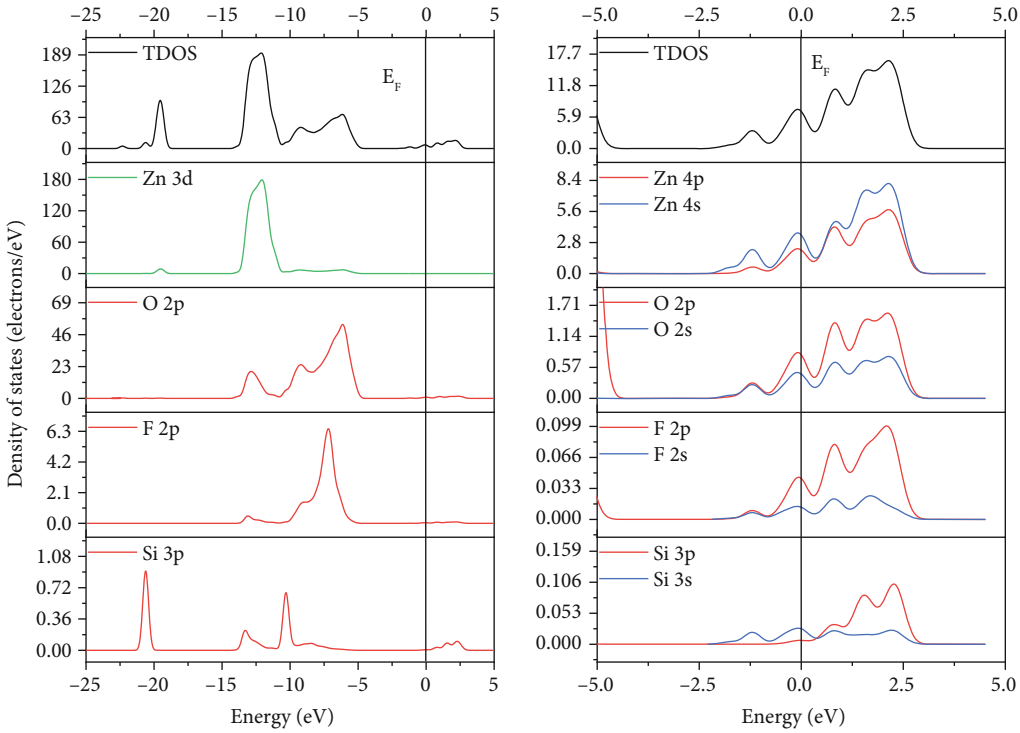


Si (1)-F (2)-ZnO

(d)

Figure 6: Continued.

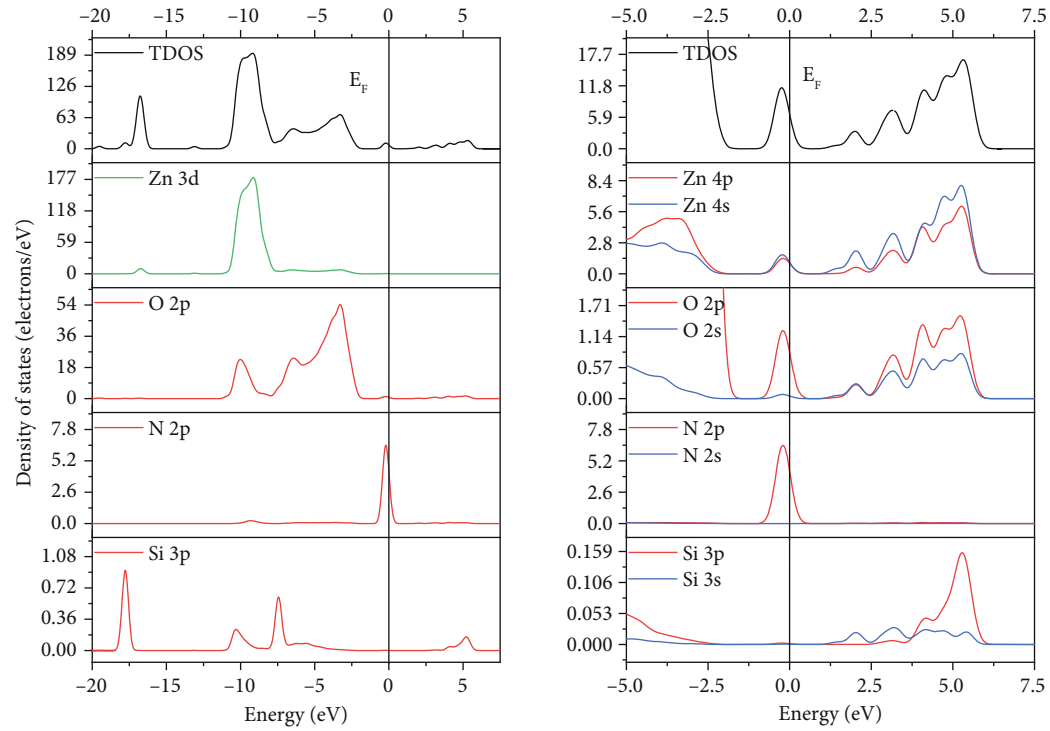


Si(1)-N(1)-ZnO

(e)

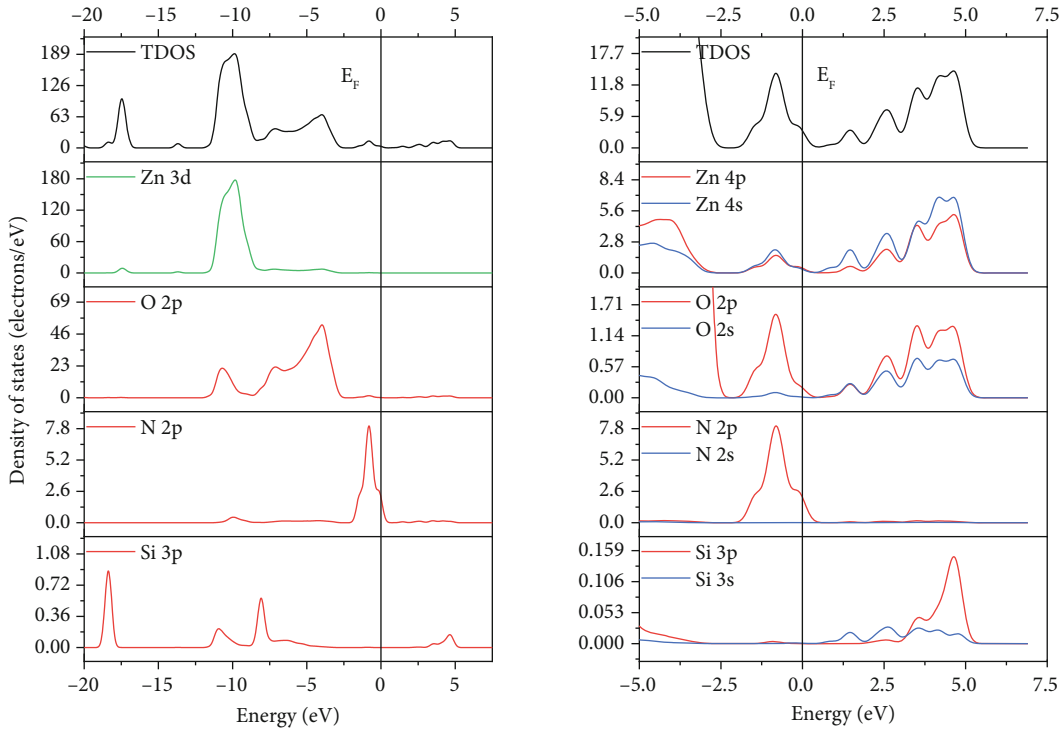


Si (1)-N (2)-ZnO

(f)

FIGURE 6: Calculated density of state for the band structure: (a) ZnO, (b) Si-ZnO with Si 1 atom, (c) Si-F-ZnO with Si and F 1 atom, (d) Si-F-ZnO with Si 1 atom and F 2 atom, (e) Si-N-ZnO with Si and N 1 atom, and (f) Si-N-ZnO with Si 1 atom and N 2 atom, respectively.

Table 3: Device parameters for the ZnO, Si-ZnO, Si-F-ZnO, and Si-N-ZnO samples: threshold voltage ($V_{th}$), field effect mobility ($\mu_{FE}$), subthreshold swing values (SS), interfacial trap density ($N_{it}$), and $I_{on}/I_{off}$ ratio.

| Condition | Cycle ratio | $V_{th}$ (V) | $\mu_{FE}$ ($cm^2$/V·s) | SS (V/decade) | $N_{it}$ ($cm^{-2}$·$eV^{-1}$) | $I_{on}/I_{off}$ |
|---|---|---|---|---|---|---|
| ZnO | - | 10.07 | 2.19$E$ + 00 | 4.38$E$ + 00 | 3.21$E$ + 13 | 1.77$E$ + 05 |
| Si-ZnO | Si-1/20 | -15.50 | 3.95$E$ + 00 | 1.46$E$ + 00 | 9.03$E$ + 12 | 5.43$E$ + 05 |
| Si-F-ZnO | Si/F-4 | -14.91 | 4.75$E$ + 00 | 8.46$E$ − 01 | 2.82$E$ + 12 | 4.81$E$ + 06 |
| | Si/F-9 | -12.86 | 4.29$E$ + 00 | 8.99$E$ − 01 | 2.15$E$ + 12 | 8.18$E$+05 |
| | Si/F-12 | -11.68 | 4.78$E$ + 00 | 6.50$E$ − 01 | 2.83$E$ + 12 | 1.29$E$ + 05 |
| | Si/F-19 | -11.16 | 5.10$E$ + 00 | 6.62$E$ − 01 | 3.26$E$ + 12 | 1.15$E$ + 05 |
| Si-N-ZnO | Si/N-4 | -4.43 | 8.67$E$ + 00 | 7.43$E$ − 01 | 3.51$E$ + 12 | 9.26$E$ + 05 |
| | Si/N-9 | -1.20 | 8.19$E$ + 00 | 7.63$E$ − 01 | 2.74$E$ + 12 | 5.29$E$ + 06 |
| | Si/N-12 | 1.05 | 1.54$E$ + 01 | 9.31$E$ − 01 | 3.13$E$ + 12 | 1.13$E$ + 06 |
| | Si/N-19 | 1.07 | 1.66$E$ + 01 | 5.98$E$ − 01 | 1.65$E$ + 12 | 4.91$E$ + 06 |

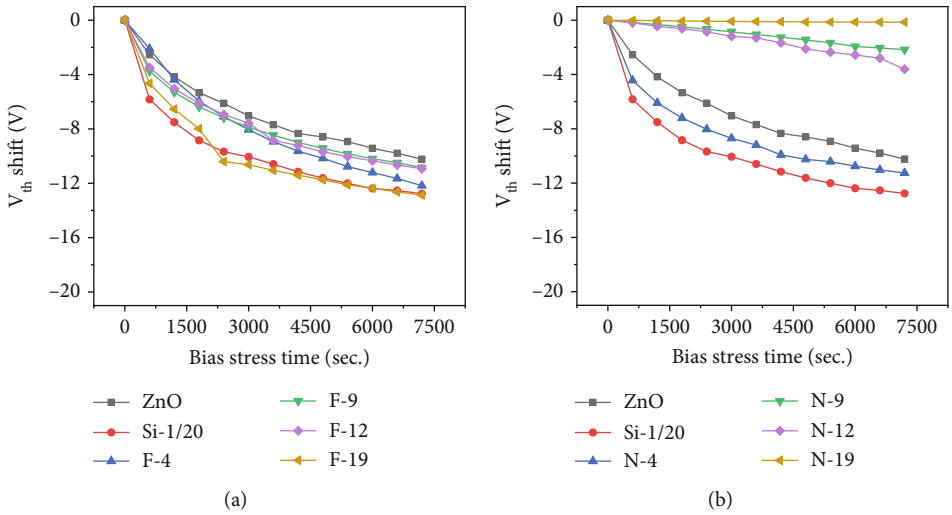


Figure 7: Time-elapsed $V_{th}$ shift in the transfer characteristic curves for (a) Si-F-ZnO and (b) Si-N-ZnO.

2.20 $cm^2$/V·s. The correlation between mobility and resistivity in the film can be expressed as [59]

$$\frac{1}{\rho} = \sigma = ne\mu, \tag{11}$$

where $\rho$, $\sigma$, $n$, $e$, and $\mu$ denote the resistivity, conductivity, carrier concentration, electron charge, and mobility, respectively.

However, the electrical tendency is opposite from that of Si-F-ZnO or Si-N-ZnO. Compared to that in Si-ZnO, the carrier concentration in Si-F-ZnO continuously increases from $1.41 \times 10^{20}$ to $4.17 \times 10^{20}$ $cm^{-3}$, whereas that of Si-N-ZnO decreases from $1.41 \times 10^{20}$ to $0.42 \times 10^{20}$ $cm^{-3}$. In other words, F acts as a donor and increases the carrier concentration in the Si-F-ZnO configuration, while N in Si-N-ZnO acts as an acceptor and decreases the carrier through charge neutralization. The resistivity of Si-F-ZnO decreases from $2.11 \times 10^{-2}$ to $0.40 \times 10^{-2}$ Ω·cm, and the mobility increases from 2.20 to 5.12 $cm^2$/V·s owing to the change in the carrier concentration in the thin film. The opposite trend is observed for Si-N-ZnO. The resistivity decreases from $2.11 \times 10^{-2}$ to $1.12 \times 10^{-2}$ Ω·cm, and the mobility increases from 2.20 to 19.15 $cm^2$/V·s. The abovementioned conductivity equation effectively explains this behavior in thin films.

*3.6. Device Properties.* Figure S8 shows the sweep characteristics of the I-V operation for the ZnO device in the $V_{gs}$ range of -50 to 50 V. It can be seen that the ion increases as the $V_d$ voltage increases to 0.1, 0.5, and 1.0 V. Therefore, it was confirmed that the device was operated in the type of n-channel enhancement as demonstrated for positive gate voltage to induce a conducting channel.

Figure S9 shows the transfer curve for a drain voltage ($V_{ds}$) of 0.1 V under the NBIS as a function of the stress time in all conditions. The TFT parameters, summarized in

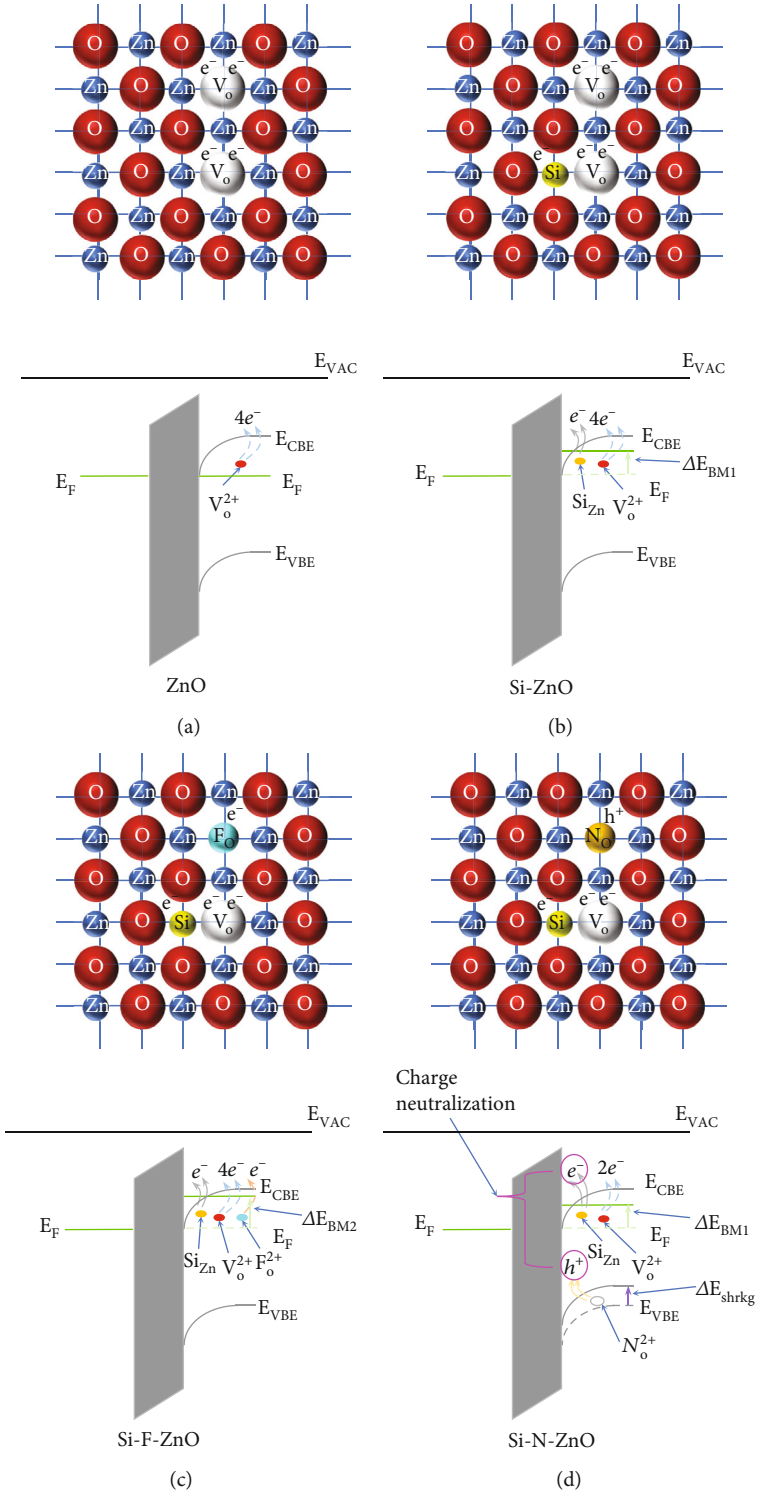


FIGURE 8: Defect distribution for specific charge carriers in the lattice and energy band structures for the devices (a) ZnO, (b) Si-ZnO (c) Si-F-ZnO, and (d) Si-N-ZnO.

Table 3, were extracted using the conventional MOSFET equation in the saturation region [60].

$$I_{ds} = \frac{W}{2L}\mu_{sat}C_{ox}\left(V_{gs-}V_{th}\right)^2, \tag{12}$$

where $W$ and $L$ denote the channel width and length, respectively, and $\mu_{sat}$, $C_{ox}$, $V_{th}$, and $V_{gs}$ denote the field-effect mobility in the saturation region, gate oxide capacitance per unit area, threshold voltage, and gate-source voltage, respectively.

The subthreshold swing (SS) slope is improved (lowered) compared with that in the ZnO case. A low SS can help turn on the device faster with a low voltage difference. In this study, the device SS reduces with anion/cation codoping, attributable to the decrease in the interfacial trap density ($N_{it}$) around the semiconductor-insulator interface according to the following relation [61]:

$$N_{it} = \left(\frac{SS \bullet \log(e)}{k_B T/q} - 1\right)\frac{C}{q}, \quad (13)$$

where $q$, $k_B$, $T$, and $t_{ch}$ denote the electron charge, Boltzmann's constant, channel layer, absolute temperature, and film thickness, respectively. The calculated $N_{it}$ values are presented in Table 2.

The initial $V_{th}$ of the ZnO case is extremely low (negative) and thus unsuitable for ordinary device driving. Moreover, $V_{th}$ in Si-ZnO is negatively shifted compared to that in the initial ZnO case. This tendency of $V_{th}$ is likely caused by the carrier concentration variation. The relation between the carrier concentration and $V_{th}$ can be expressed as [62]

$$I_{ds_{sat}} = \frac{W \bullet t}{L}\sigma \bullet V_{ds_{sat}}, \quad (14)$$

where $V_{ds\_sat}$ is the saturation drain voltage, $I_{ds\_sat}$ is the corresponding saturation current, $\sigma$ is the conductivity of the channel layer, $t$ is the thickness, and $W$ and $L$ are the channel width and length, respectively. The electrical conductivity is directly related to the carrier concentration as follows [62]:

$$N_e = \frac{\sigma}{q \bullet \mu}, \quad (15)$$

where $\mu$ is the field-effect mobility of TFTs in the saturation region, $N_e$ is the channel carrier concentration, and $q$ is the electronic charge ($1.6 \times 10^{-19}$ C). As the carrier concentration in the semiconductor increases, thereby decreases the threshold voltage of n-type oxide semiconductor TFTs [63, 64]. In cases with F or N codoping, $V_{th}$ shifts positively compared with those in the Si-ZnO condition. In other words, the passivation effect of the oxygen vacancy caused by F or N codoping decreases the leakage current in the device [65]. Furthermore, $V_{th}$ in the Si-N-ZnO case exhibits a higher positive shift because the passivation efficiency of N codoping is slightly higher than that of F codoping.

Figure 7 shows the $V_{th}$ shift for each case under NBIS over time for each codoping condition. The $V_{th}$ shift of Si-F-ZnO (Figure 7(a)) decreases slightly from the Si/F-4 to Si/F-12 conditions and then increases in the Si/F-19 case. These findings indicate that the carrier concentration is high in this case owing to $V_O$ passivation caused by F codoping. As discussed, the charge carriers generated by $V_O$ ionization and electrons provided by $V_O$ passivation by F doping (Equations (4) and (6)) enhance the conduction properties in the conduction band, causing $V_{th}$ to decrease. In contrast, the $V_{th}$ shift in the Si-N-ZnO cases (Figure 7(b)) decreases as the N doping concentration increases and finally converges to zero in the Si/N-19 case. The stabilization of $V_{th}$ is attributable to $V_O$ passivation by N codoping and reduced carrier concentration by charge compensation. Because the orbital energy of N 2p is higher than that of O 2p, the $V_O$ passivation effect of N doping shifts the valence band upward toward $E_F$ and covers $V_O$, thereby enhancing the $V_{th}$ shift characteristics.

In conclusion, Si, as a cation dopant near the CBM, increases the carrier concentration and decreases SS by decreasing the interfacial trap density. F or N as similar anion dopants near the VBM leads to oxygen vacancy passivation, although the electrical properties of the corresponding devices are different. F, despite the anion, increases the carrier concentration and leads to a negative shift in $V_{th}$. Consequently, $\mu_{FE}$ is saturated by the scattering effect. In contrast, N acts as a carrier suppressor, thereby increasing $\mu_{FE}$ and leading to a positive shift in $V_{th}$ because of the decreased carrier concentration. In other words, F has a less effective $V_O$ passivation effect than N, and the improvement of $V_{th}$ for NBIS due to carrier concentration increases is small. On the other hand, N reduces charge carriers in the device while blocking $V_O$ generation through energy-wise formation of N 2p, resulting in an improvement in $V_{th}$ under the NBIS environment. Figure 8 shows the device energy band structure for the given parameter values, doping conditions, and defect substitution.

Figure 8(a) shows that ZnO is an intrinsic n-type semiconductor with naturally generated $V_O$. Owing to Si doping into the ZnO films, the carrier concentration increases owing to the substitution of Si in the Zn sites and the formation of $V_O$ (Figure 8(b)). As shown in Figure 8(c), although the F dopant replaces $V_O$ in the Si-F-ZnO case, the increased charge carrier concentration from F doping and $V_O$ ionization might limit the improvement in the $V_{th}$ characteristics. In contrast, in the case of Si-N-ZnO, the $V_{th}$ shift converges to zero because $V_O$ might be covered with the shifting of the valence band energy toward $E_F$ (reduction in $E_g$), and illumination would not generate the additional charge carrier generation, as shown in Figure 8(d).

## 4. Conclusions

The effect of cation (Si) and anion (F or N) codoping on films formed using ALD was investigated, and the stress stability characteristics of the corresponding devices subjected to oxygen annealing treatment were explored. All the conditioned films exhibited hexagonal wurtzite structures with the preferred (100) orientation owing to the hindering process. According to the XPS analysis, Si doping caused Zn site substitution and $V_O$ generation, and both F and N exerted a passivation effect on $V_O$, although the dopants differed in terms of their effect on the charge carrier concentration. The BM effect caused the widening of $E_{g\_opt}$ in the cases of Si doping and F codoping, although bandgap shrinkage was confirmed in the case of N codoping. The differences in the bandgap variance and carrier concentration could be explained by the band structure obtained from the density of states calculations. The initial device characteristics and $V_{th}$ shift under the NBIS condition over time were measured. Compared to that in ZnO, SS was lowered by doping

with Si because the interfacial trap density in the thin film decreased. Si helped enhance the carrier concentration and reduce the trap density, and both F and N exhibited a passivation effect for the oxygen vacancy. In terms of the effect of the anions on the device stability characteristics, N corresponded to a superior $V_O$ passivation effect, improved mobility, and higher $V_{\text{th}}$ stability compared with those of F.

## Data Availability

Data will be made available on request.

## Conflicts of Interest

The authors declare that they have no known competing financial interests or personal relationships that could have appeared to influence the work reported in this paper.

## Acknowledgments

This work was supported by the National Research Foundation of Korea (NRF) grant funded by the Korean government (MSIT) (grant nos. RS-2023-00208801 and NRF-2022M3F3A2A01044952).

## Supplementary Materials

Supplementary information for this article includes ellipsometry, O 1s XPS, UV transmittance and Tauc's plot results, and Hall measurement for Si-F-ZnO and Si-N-ZnO samples. Electronic band structure and transfer characteristic curves for ZnO, Si-ZnO, Si-F-ZnO, and Si-N-ZnO samples. The crystalline parameters and bonding characteristics of oxygen for ZnO, Si-ZnO, Si-F-ZnO, and Si-N-ZnO samples are given in Tables S1 and S2. *(Supplementary Materials)*

## References

[1] T. Ramachandran, G. Anandkumar, L. M. Azarudeen, and K. Vishista, "Structural, morphology and luminescence studies on Mn-doped ZnO phosphor," *Engineering and Medicine*, vol. 6, no. 11, pp. 1205–1209, 2014.

[2] H.-D. Kim, J. H. Kim, K. Park et al., "Effects of fluorine doping on the electrical performance of ZnON thin-film transistors," *ACS Applied Materials & Interfaces*, vol. 9, no. 29, pp. 24688–24695, 2017.

[3] S. Lee, A. Nathan, S. Jeon, and J. Robertson, "Oxygen defect-induced metastability in oxide semiconductors probed by gate pulse spectroscopy," *Scientific Reports*, vol. 5, no. 1, p. 14902, 2015.

[4] T. Kim, M. J. Kim, J. Lee, and J. K. Jeong, "Boosting carrier mobility in zinc oxynitride thin-film transistors via tantalum oxide encapsulation," *ACS Applied Materials & Interfaces*, vol. 11, no. 25, pp. 22501–22509, 2019.

[5] R. E. Treharne, L. J. Phillips, K. Durose, A. Weerakkody, I. Z. Mitrovic, and S. Hall, "Non-parabolicity and band gap renormalisation in Si doped ZnO," *Journal of Applied Physics*, vol. 115, no. 6, 2014.

[6] T. Tohsophon, J. Hüpkes, S. Calnan et al., "Damp heat stability and annealing behavior of aluminum doped zinc oxide films prepared by magnetron sputtering," *Thin Solid Films*, vol. 511, pp. 673–677, 2006.

[7] B. Sang, K. Kushiya, D. Okumura, and O. Yamase, "Performance improvement of CIGS-based modules by depositing high-quality Ga-doped ZnO windows with magnetron sputtering," *Solar Energy Materials & Solar Cells*, vol. 67, no. 1-4, pp. 237–245, 2001.

[8] K.-M. Kang, Y. Wang, M. Kim, and H.-H. Park, "Study on properties of Ga/F-co-doped ZnO thin films prepared using atomic layer deposition," *Thin Solid Films*, vol. 660, pp. 913–919, 2018.

[9] C. N. R. Rao and F. L. Deepak, "Absence of ferromagnetism in Mn- and co-doped ZnO," *Journal of Materials Chemistry*, vol. 15, no. 5, pp. 573–578, 2005.

[10] J. G. Lu, Z. Z. Ye, F. Zhuge, Y. J. Zeng, B. H. Zhao, and L. P. Zhu, "p -Type conduction in N–Al co-doped ZnO thin films," *Applied Physics Letters*, vol. 85, no. 15, pp. 3134-3135, 2004.

[11] J. Beltrán, J. Osorio, C. Barrero, C. B. Hanna, and A. Punnoose, "Magnetic properties of Fe doped, Co doped, and Fe+ Co co-doped ZnO," *Journal of Applied Physics*, vol. 113, no. 17, article 17C308, 2013.

[12] Z. Ma, W. Zhao, and Y. Wang, "Electrical properties of Na/Mg co-doped ZnO thin films," *Thin Solid Films*, vol. 515, no. 24, pp. 8611–8614, 2007.

[13] T. Minami, H. Sato, H. Nanto, and S. Takata, "Highly conductive and transparent silicon doped zinc oxide thin films prepared by RF magnetron sputtering," *Japanese Journal of Applied Physics*, vol. 25, no. 9A, pp. L776–L779, 1986.

[14] B. Cordero, V. Gómez, A. E. Platero-Prats et al., "Covalent radii revisited," *Dalton Transactions*, vol. 21, pp. 2832–2838, 2008.

[15] D. Das and L. Karmakar, "Optimization of Si doping in ZnO thin films and fabrication of n-ZnO:Si/p-Si heterojunction solar cells," *Journal of Alloys and Compounds*, vol. 824, p. 153902, 2020.

[16] H.-C. Wu, Y.-C. Peng, and T.-P. Shen, "Electronic and optical properties of substitutional and interstitial Si-doped ZnO," *Materials*, vol. 5, no. 11, pp. 2088–2100, 2012.

[17] Y.-J. Choi and H.-H. Park, "A simple approach to the fabrication of fluorine-doped zinc oxide thin films by atomic layer deposition at low temperatures and an investigation into the growth mode," *Journal of Materials Chemistry C*, vol. 2, no. 1, pp. 98–108, 2014.

[18] R. Kumari, A. Sahai, and N. Goswami, "Effect of nitrogen doping on structural and optical properties of ZnO nanoparticles," *Progress in Natural Science: Materials International*, vol. 25, no. 4, pp. 300–309, 2015.

[19] G. Xing, L. Zhao, T. Sun, Y. Su, and X. Wang, "Hydrothermal derived nitrogen doped SrTiO3 for efficient visible light driven photocatalytic reduction of chromium (VI)," *SpringerPlus*, vol. 5, no. 1, p. 1132, 2016.

[20] H. Wang, H. P. Ho, and J. B. Xu, "Photoelectron spectroscopic investigation of nitrogen chemical states in ZnO: (N,Ga) thin films," *Journal of Applied Physics*, vol. 103, no. 10, p. 103704, 2008.

[21] S. Lee, A. Nathan, Y. Ye, Y. Guo, and J. Robertson, "Localized tail states and electron mobility in amorphous ZnON thin film transistors," *Scientific Reports*, vol. 5, no. 1, p. 13467, 2015.

[22] S. J. Lim, S.-J. Kwon, H. Kim, and J.-S. Park, "High performance thin film transistor with low temperature atomic layer deposition nitrogen-doped ZnO," *Applied Physics Letters*, vol. 91, no. 18, p. 183517, 2007.

[23] J. Yang, A. Bahrami, X. Ding et al., "Low-temperature atomic layer deposition of high-kSbOxfor thin film transistors," *Advanced Electronic Materials*, vol. 8, no. 7, p. 2101334, 2022.

[24] J. Yang, J. Li, A. Bahrami et al., "Wafer-scale growth of Sb2Te3films via low-temperature atomic layer deposition for self-powered photodetectors," *ACS Applied Materials & Interfaces*, vol. 14, no. 48, pp. 54034–54043, 2022.

[25] B. D. Ahn, D.-w. Choi, C. Choi, and J.-S. Park, "The effect of the annealing temperature on the transition from conductor to semiconductor behavior in zinc tin oxide deposited atomic layer deposition," *Applied Physics Letters*, vol. 105, no. 9, 2014.

[26] L. Dong, Q.-Q. Sun, Y. Shi et al., "Initial reaction mechanism of nitrogen-doped zinc oxide with atomic layer deposition," *Thin Solid Films*, vol. 517, no. 15, pp. 4355–4359, 2009.

[27] J. P. Perdew, K. Burke, and M. Ernzerhof, "Generalized gradient approximation made simple," *Physical Review Letters*, vol. 77, no. 18, pp. 3865–3868, 1996.

[28] J. P. Perdew, M. Ernzerhof, and K. Burke, "Rationale for mixing exact exchange with density functional approximations," *The Journal of Chemical Physics*, vol. 105, no. 22, pp. 9982–9985, 1996.

[29] G. Kresse and J. Hafner, "Ab initiomolecular-dynamics simulation of the liquid-metal–amorphous-semiconductor transition in germanium," *Physical Review B: Condensed Matter*, vol. 49, no. 20, pp. 14251–14269, 1994.

[30] G. Kresse and J. Hafner, "Ab initiomolecular dynamics for liquid metals," *Physical Review B: Condensed Matter*, vol. 47, no. 1, pp. 558–561, 1993.

[31] A. Janotti and C. G. Van De Walle, "Native point defects in ZnO," *Physical Review B*, vol. 76, no. 16, 2007.

[32] F. Shan, B. Shin, S. Jang, and Y. Yu, "Substrate effects of ZnO thin films prepared by PLD technique," *Journal of the European Ceramic Society*, vol. 24, no. 6, pp. 1015–1018, 2004.

[33] S.-Y. Pung, K.-L. Choy, X. Hou, and C. Shan, "Preferential growth of ZnO thin films by the atomic layer deposition technique," *Nanotechnology*, vol. 19, no. 43, p. 435609, 2008.

[34] Z. Baji, Z. Lábadi, Z. E. Horváth et al., "Nucleation and growth modes of ALD ZnO," *Crystal Growth & Design*, vol. 12, no. 11, pp. 5615–5620, 2012.

[35] J. Yang, A. Bahrami, X. Ding et al., "Characteristics of ALD-ZnO thin film transistor using H2O and H2O2as oxygen sources," *Advanced Materials Interfaces*, vol. 9, no. 15, p. 2101953, 2022.

[36] P. Singh, A. Kumar, A. Kaushal, D. Kaur, A. Pandey, and R. Goyal, "In situ high temperature XRD studies of ZnO nanopowder prepared via cost effective ultrasonic mist chemical vapour deposition," *Bulletin of Materials Science*, vol. 31, no. 3, pp. 573–577, 2008.

[37] X. Chen, X. Wang, and D. Fang, "A review on C1s XPS-spectra for some kinds of carbon materials," *Nanotubes and Carbon Nanostructures*, vol. 28, no. 12, pp. 1048–1058, 2020.

[38] M. Wang, L. Jiang, E. J. Kim, and S. H. Hahn, "Electronic structure and optical properties of Zn(OH)2: LDA+U calculations and intense yellow luminescence," *RSC Advances*, vol. 5, no. 106, pp. 87496–87503, 2015.

[39] Y. Liu, J. Shen, Z. Chen, L. Yang, Y. Liu, and Y. Han, "Effects of amorphous-zinc-silicate-catalyzed ozonation on the degradation of p-chloronitrobenzene in drinking water," *Appl Catal a-Gen*, vol. 403, no. 1-2, pp. 112–118, 2011.

[40] I. Suzuki, T. Omata, Y. Shiratsuchi, R. Nakatani, N. Kitamura, and S. Otsuka-Yao-Matsuo, "Fabrication of ZnF2 thin films and their vacuum ultraviolet transparency," *Thin Solid Films*, vol. 534, pp. 508–514, 2013.

[41] D. G. Georgiev, J. P. Moening, S. Naleshwar, and A. H. Jayatissa, *IEEE nanotechnology materials and devices conference*, IEEE, 2009.

[42] J. Lee, S. Y. Lee, H. Y. Jeong, and S. O. Cho, "Oxygen Content-Controllable Synthesis of Non-Stoichiometric Silicon Suboxide Nanoparticles by Electrochemical Anodization," *Nanomaterials (Basel)*, vol. 10, no. 11, p. 2137, 2020.

[43] J. L. Lyons, A. Janotti, and C. G. Van De Walle, "Role of Si and Ge as impurities in ZnO," *Physical Review B*, vol. 80, no. 20, 2009.

[44] A. K. Das, P. Misra, and L. M. Kukreja, "Effect of Si doping on electrical and optical properties of ZnO thin films grown by sequential pulsed laser deposition," *Journal of Physics D: Applied Physics*, vol. 42, no. 16, p. 165405, 2009.

[45] W. Körner and C. Elsässer, "Density functional theory study for polycrystalline ZnO doped with Si or Nb," *Physical Review B*, vol. 83, no. 20, 2011.

[46] J. Clatot, G. Campet, A. Zeinert, C. Labrugère, M. G. Nistor, and A. Rougier, "Low temperature Si doped ZnO thin films for transparent conducting oxides," *Solar Energy Materials & Solar Cells*, vol. 95, no. 8, pp. 2357–2362, 2011.

[47] H. Yuan, "Structural, electrical and optical properties of Si doped ZnO films grown by atomic layer deposition," *Journal of Materials Science: Materials in Electronics*, vol. 23, no. 11, pp. 2075–2081, 2012.

[48] C. Hong, K.-M. Kang, M. Kim et al., "Structural, electrical, and optical properties of Si-doped ZnO thin films prepared via supercycled atomic layer deposition," *Materials Science and Engineering: B*, vol. 273, p. 115401, 2021.

[49] B. H. Lee, D.-Y. Lee, J. Y. Lee, S. Park, S. Kim, and S. Y. Lee, "Investigation on the improvement of stability of nitrogen doped amorphous SiInZnO thin-film transistors," *Solid-State Electronics*, vol. 158, pp. 59–63, 2019.

[50] W. Chen, Q.-Q. Sun, S.-J. Ding, D. W. Zhang, and L.-K. Wang, "First principles calculations of oxygen vacancy passivation by fluorine in hafnium oxide," *Applied Physics Letters*, vol. 89, no. 15, p. 152904, 2006.

[51] J. Zhang, Y. Wang, S. Zheng, H. Xue, and H. Pang, "N-Doped mesoporous ZnO with oxygen vacancies for stable hydrazine electrocatalysis," *ChemNanoMat*, vol. 5, no. 1, pp. 79–84, 2019.

[52] Y.-J. Choi, K.-M. Kang, and H.-H. Park, "Anion-controlled passivation effect of the atomic layer deposited ZnO films by F substitution to O-related defects on the electronic band structure for transparent contact layer of solar cell applications," *Solar Energy Materials & Solar Cells*, vol. 132, pp. 403–409, 2015.

[53] D. C. Look, "Recent advances in ZnO materials and devices," *Materials Science and Engineering B*, vol. 80, no. 1-3, pp. 383–387, 2001.

[54] J. B. Coulter and D. P. Birnie, "Assessing Tauc Plot Slope Quantification: ZnO Thin Films as a Model System," *Physica Status Solidi (b)*, vol. 255, no. 3, article 1700393, 2018.

[55] T. G. Mayerhçfer, H. Mutschke, and J. Popp, "Employing Theories Far beyond Their Limits—The Case of the (Boguer-) Beer–Lambert Law," *ChemPhysChem*, vol. 17, no. 13, pp. 1948–1955, 2016.

[56] K. J. Kim and Y. R. Park, "Large and abrupt optical band gap variation in In-doped ZnO," *Applied Physics Letters*, vol. 78, no. 4, pp. 475–477, 2001.

[57] K.-M. Kang, Y.-J. Choi, G. Y. Yeom, H.-H. Park, and J. Vac, "Thickness-dependent growth orientation of F-doped ZnO films formed by atomic layer deposition," *Journal of Vacuum Science & Technology A*, vol. 34, no. 1, 2016.

[58] L. Franklin, C. E. Ekuma, G. L. Zhao, D. Bagayoko, and J. Phys, "Density functional theory description of electronic properties of wurtzite zinc oxide," *Journal of Physics and Chemistry of Solids*, vol. 74, no. 5, pp. 729–736, 2013.

[59] J. Hong, K.-i. Katsumata, and N. Matsushita, "High-conductivity solution-processed ZnO films realized via UV irradiation and hydrogen treatment," *Acta Materialia*, vol. 103, pp. 844–849, 2016.

[60] D. A. Neamen, *Semiconductor Physics and Devices: Basic Principles*, McGraw-hill, 2003.

[61] K.-Y. Chen, C.-C. Yang, C.-Y. Huang, and Y.-K. Su, "ALD Al2O3gate dielectric on the reduction of interface trap density and the enhanced photo-electric performance of IGO TFT," *RSC Advances*, vol. 10, no. 17, pp. 9902–9906, 2020.

[62] L.-C. Liu, J.-S. Chen, J.-S. Jeng, and W.-Y. Chen, "Variation of oxygen deficiency in solution-processed ultra-thin zinc-tin oxide films to their transistor characteristics," *ECS Journal of Solid State Science and Technology*, vol. 2, no. 4, pp. Q59–Q64, 2013.

[63] J. H. Lee, P. Lin, J. C. Ho, and C. C. Lee, "Chemical solution deposition of Zn[sub 1−x]Zr[sub x]O thin films as active channel layers of thin-film transistors," *Electrochemical and Solid-State Letters*, vol. 9, no. 4, p. G117, 2006.

[64] Y. S. Rim, D. L. Kim, W. H. Jeong, and H. J. Kim, "Effect of Zr addition on ZnSnO thin-film transistors using a solution process," *Applied Physics Letters*, vol. 97, no. 23, p. 233502, 2010.

[65] S. C. Kang, S. Y. Kim, S. K. Lee et al., "Channel defect profiling and passivation for ZnO thin-film transistors," *Nanomaterials*, vol. 10, no. 6, p. 1186, 2020.